Reducing the exergy destruction in the cryogenic heat exchangers of hydrogen liquefaction processes

Øivind Wilhelmsen[a,b], David Berstad[a], Ailo Aasen[a,b], Petter Nekså[a,b], Geir Skaugen[a]

[a] *SINTEF Energy Research, Sem Sælands vei 11, NO-7034 Trondheim, Norway*
[b] *NTNU, Department of Energy and Process Engineering, Kolbjørn Hejes vei 1B, NO-7491 Trondheim, Norway*

Abstract

A present key barrier for implementing large-scale hydrogen liquefaction plants is their high power consumption. The cryogenic heat exchangers are responsible for a significant part of the exergy destruction in these plants and we evaluate in this work strategies to increase their efficiency. A detailed model of a plate-fin heat exchanger is presented that incorporates the geometry of the heat exchanger, nonequilibrium ortho-para conversion and correlations to account for the pressure drop and heat transfer coefficients due to possible boiling/condensation of the refrigerant at the lowest temperatures. Based on available experimental data, a correlation for the ortho-para conversion kinetics is developed, which reproduces available experimental data with an average deviation of 2.2%. In a plate-fin heat exchanger that is used to cool the hydrogen from 47.8 K to 29.3 K with hydrogen as refrigerant, we find that the two main sources of exergy destruction are thermal gradients and ortho-para hydrogen conversion, being responsible for 69% and 29% of the exergy destruction respectively. A route to reduce the exergy destruction from the ortho-para hydrogen conversion is to use a more efficient catalyst, where we find that a doubling of the catalytic activity in comparison to ferric-oxide, as demonstrated by nickel oxide-silica catalyst, reduces the exergy destruction by 9%. A possible route to reduce the exergy destruction from thermal gradients is to employ an evaporating mixture of helium and neon at the cold-side of the heat exchanger, which reduces the exergy destruction by 7%. We find that a combination of hydrogen and helium-neon as refrigerants at high and low temperatures respectively, enables a reduction of the exergy destruction by 35%. A combination of both improved catalyst and the use of hydrogen and helium-neon as refrigerants gives the possibility to reduce the exergy destruction in the cryogenic heat exchangers by 43%. The limited efficiency of the ortho-para catalyst represents a barrier for further improvement of the efficiency.

Keywords: Hydrogen, Liquefaction, Heat exchanger, plate-fin, ortho-hydrogen, para-hydrogen, catalyst, ortho-para reaction kinetics

1. Introduction

Hydrogen represents a zero-emission fuel when used, for instance, in fuel cells for mobility or electricity generation. The only components emitted from these fuel cells are heat and water. The most common way to produce hydrogen is by reforming of natural gas (48%), but a large portion is also produced from oil (30%) and by coal gasification (18%) [1]. When steam-methane reforming, or other reforming technologies such as partial oxidation or auto-thermal reforming, is combined with pre-combustion CO_2 capture and storage, the processes can be used to provide a clean energy carrier for transportation or for generating electricity. On a long-term, a gradual conversion to a hydrogen-based society can be a way of mitigating the threat of accelerated global warming from anthropogenic greenhouse gas emissions.

Some of the largest technological challenges in a transition to a hydrogen-society are associated with the transport and storage of hydrogen. Hydrogen can either be liquefied (e.g. at 1.3 bar and 21 K), or compressed (typically in the range 200–700 bar and near ambient temperature). The preferred method of transportation depends on different circumstances such as the quantity of hydrogen, the distance of transportation and the preferred state of distribution and end use. The advantage with liquefied hydrogen (LH_2) is that the energy density is almost 4.5 times larger than compressed hydrogen at 200 bar [2, 3]. This reduces the necessary volume and weight of storage-facilities, which becomes particularly attractive if large quantities of hydrogen are going to be transported from remote locations and for distribution to filling stations in cities.

How beneficial liquefaction of hydrogen will be in comparison to compressed hydrogen depends to a large extent on how energy and cost efficient the hydrogen liquefaction process can be made. One of the current barriers for implementing large-scale plants for liquefaction of hydrogen is their high power consumption. The exergy efficiency of existing liquefaction plants is relatively low (25%–30% when factoring in the penalty for externally supplied liquid nitrogen for pre-cooling) and there is a large potential for improvement [4]. In currently operating hydrogen liquefaction plants, the specific energy requirement to liquefy hydrogen is 11.9 kWh/kg LH_2 for the Leuna plant [5], and slightly lower for newer plants. Several works have in recent years proposed novel solutions for lowering the specific energy requirements of the hydrogen liquefaction pro-

Email address: oivind.wilhelmsen@ntnu.no (Øivind Wilhelmsen)

cess [5–9]. The typical hydrogen liquefaction process consists of four consecutive stages [5, 10]:

Stage 1: Pre-compression of the hydrogen feed gas, if required.

Stage 2: Pre-cooling of the hydrogen gas to about 80 K.

Stage 3: Cryogenic cooling of the hydrogen gas down to 20 K–30 K, including ortho-to-para-hydrogen conversion.

Stage 4: Final expansion and liquefaction of the hydrogen.

The processes presented in the literature differ most significantly in the pre-cooling and cryogenic cooling stages (Stage 2 and 3). Most of the current technology for hydrogen liquefaction is characterized by the nature of the refrigeration cycle that is used in the cryogenic refrigeration section, i.e. whether a Claude cycle or a reverse Brayton cycle has been employed [10].

Small-to mid-scale hydrogen liquefaction plants are often placed in close vicinity to cryogenic air separation facilities such that liquid nitrogen can be used as refrigerant in the pre-cooling stage. Due to the limited global requirement for pure oxygen, liquefied nitrogen will not be available as a cheap refrigerant for future large-scale hydrogen liquefaction plants.

The most energy and cost efficient processes suggested in the literature [5, 8, 9], use mixed refrigerants instead of nitrogen to precool the hydrogen, where the mixed refrigerant consists of hydrocarbons, nitrogen and possibly other components such as neon [5]. A mixed refrigerant can have a tailor-made composition to enable a tight thermal match in the heat exchangers, leading to higher efficiency in the pre-cooling stage (Stage 2). The recent works by Berstad et. al. [5], the IDEALHY-consortium [8] and Cardella et al. [9], present processes with very high overall energy efficiencies. In some of these processes, mixtures with neon in combination with either hydrogen or helium are used as refrigerants in the cryogenic cooling stage (Stage 3). One advantage of including neon in the mixture, is that neon increases the molecular weight of the mixture, such that conventional turbo compressors can be used with a maximum of 6 to 8 stages [9]. Turbo compressors can easily be up scaled, and have generally higher efficiency and throughput capacity than oil-free piston compressors, which in overall can enable more efficient processes. Another advantage of using neon-mixtures at low temperatures is the enhanced heat transfer coefficient due to evaporating/condensing refrigerant.

There are currently knowledge gaps that need to be closed, both to realize the novel concepts proposed in the literature [5–9], and to develop even more energy efficient hydrogen liquefaction processes. For instance, it is crucial to have a tight thermal match between the hydrogen and the refrigerant, in particular at the lowest temperatures due to the otherwise high exergy destruction. An additional necessity in the hydrogen liquefaction process is to include catalyst to convert ortho- to para-hydrogen (the protons in the H_2 molecule spin in the same (ortho) or in opposite directions (para)). Otherwise, the heat that is generated when liquefied ortho-hydrogen converts to para-hydrogen in e.g. storage tanks will lead to full evaporation, since the enthalpy difference of ortho-para conversion exceeds the latent heat of evaporation at low temperatures. The ortho to para conversion requires energy-demanding refrigeration, and the exergy destruction increases at decreasing temperature. The required conversion of ortho to para hydrogen is in modern liquefaction plants carried out continuously by filling the plate-fin heat exchangers with catalyst [11].

In this work, we evaluate strategies to reduce the exergy destruction and entropy production in the cryogenic plate-fin heat exchangers in a hydrogen liquefaction facility by taking advantage of a detailed mathematical model that incorporates the most important physical phenomena. To the best of our knowledge, such an analysis has not been presented before in the literature. We present first the model in Sec. 2. Different cases are defined in Sec. 3, where the cases differ in design parameters and choice of refrigerant. Results and discussion are presented in Sec. 4 with concluding remarks in Sec. 5.

2. Theory

First, a steady-state, distributed mathematical model that describes a plate-fin heat exchanger for liquefaction of hydrogen will be presented. The heat exchanger consists of alternating layers with hot and cold streams, where some of the layers are filled with catalyst to speed up the kinetics of the following spin-isomer reaction:

$$\mathrm{H_{2,o}} \rightleftharpoons \mathrm{H_{2,p}}, \tag{1}$$

where subscripts o and p refer to ortho and para hydrogen.

2.1. Mass balances

Plate fin heat exchangers consist of alternating hot and cold streams, which comprise a repeating unit. If boundary effects are neglected, the behavior of the overall heat exchanger can be represented by considering a number n_r, of hot and cold streams that sequentially make up the full plate-fin heat exchanger that has $n = n_r N$ number of streams, where N is the number of times the sequence is repeated. In the layers with catalyst where the reaction in Eq. 1 occurs, the steady-state molar balance of para-hydrogen gives:

$$\frac{\mathrm{d}\dot{m}_{H_2,\mathrm{p}}}{\mathrm{d}z} = A_{H_2}\eta\, r_{\mathrm{o}\rightarrow\mathrm{p}}, \tag{2}$$

where $\dot{m}_{H_2,\mathrm{p}}$ is the mass flow rate of para hydrogen, z is the spatial dimension, A_{H_2} is the cross section area of a layer with catalyst pellets, η is the effectiveness factor and $r_{\mathrm{o}\rightarrow\mathrm{p}}$ is the reaction rate per reactor volume per second for the forward reaction in Eq. 1. The effectiveness factor, $\eta \in [0, 1]$ incorporates that the ortho to para conversion occurs on the surfaces of the catalyst, where the resistance to mass or heat transfer in the catalyst pellets decreases the reaction rate in comparison to bulk-conditions. Since the catalyst pellets considered in this work are of small dimensions, we have assumed $\eta = 1$. Hutchinson et al. [12] compared expressions to describe the reaction rate for the ortho-para conversion, and found that the following expression was capable of representing the reaction rate of both the

forward and the backward reaction in Eq. 1 to a good accuracy:

$$r_{o\to p} = K \ln\left[\left(\frac{x_{H_2,\mathrm{p}}}{x^{\mathrm{eq}}_{H_2,\mathrm{p}}}\right)^n \left(\frac{1-x^{\mathrm{eq}}_{H_2,\mathrm{p}}}{1-x_{H_2,\mathrm{p}}}\right)\right], \tag{3}$$

where n and K are parameters, x is the mole fraction and superscript eq refers to the equilibrium value. In Sec. 4.1, we shall use available experimental data [13–15] to correlate K and n as functions of the reduced temperature and pressure. The equilibrium mole fraction of para hydrogen can either be obtained by identifying the minimum Gibbs energy of the Equations of State (EoS) by Leachman et al. [2], or by using the following correlation [16]:

$$\begin{aligned} x^{\mathrm{eq}}_{H_2,\mathrm{p}} =& 0.1\left[\exp\left(\frac{-5.313}{\tau}\right)+0.1\right]^{-1} - 2.52\cdot 10^{-4}\tau^3 \\ &+ 3.71\cdot 10^{-3}\tau^2 - 2.04\cdot 10^{-3}\tau - 0.00227, \end{aligned} \tag{4}$$

which reproduces experimental data on the ortho-para equilibrium within their accuracy between 5 K–300 K. Here, $\tau = T/T_c$ where T_c is the critical temperature of normal hydrogen, provided in Tab. 3.

2.2. Energy balances

For layer j of a plate-fin heat exchanger, located between the layers $j-1$ and $j+1$, the steady-state energy balances can be represented as:

$$\frac{dh_j}{dz} = \frac{\gamma_j}{2\dot{m}_j}\left(J_{q,j-1,j} + J_{q,j+1,j}\right). \tag{5}$$

Here, h_j denotes the specific enthalpy, $\dot{m}_j$ the mass flow-rate, γ_j the perimeter within layer k and $J_{q,i,j}$ denotes the heat flux from stream i to stream j, where $J_{q,i,j} = -J_{q,j,i}$. The factor $(1/2)$ in Eq. 5 reflects that the perimeter of a layer interacts with two other layers, the layer above and the layer below, where half of the overall perimeter is attributed to each. The advantage of formulating the energy balances in terms of the enthalpy of the stream, is that any enthalpy changes that come from phase-changes or chemical reactions are automatically taken into account and do not have to be explicitly incorporated into the equation, e.g. by an enthalpy of reaction term. This is in contrast to when the energy balance is formulated in terms of differential equations for the temperature.

At each position, the temperature within a layer can be obtained by performing phase equilibrium calculations where the enthalpy and pressure are specified, as described in Ref. [17]. In this work, we used a nested loop approach to solve the enthalpy-pressure phase equilibrium calculations [18], employing the thermodynamic framework presented in Ref. [19]. The layers with ortho- and para-hydrogen were described as an ideal mixture between ortho and para-hydrogen at local equilibrium at each position z, where the EoS by Leachman et al. [2] was used to describe the thermodynamic properties of ortho and para hydrogen. Other refrigerants were described by the Peng-Robinson EoS [20]. The temperature of the layers with catalyst and a nonequilibrium mixture of ortho-para hydrogen were found by using Eq. 5 and simultaneously requiring the same temperature and pressure for ortho and para hydrogen.

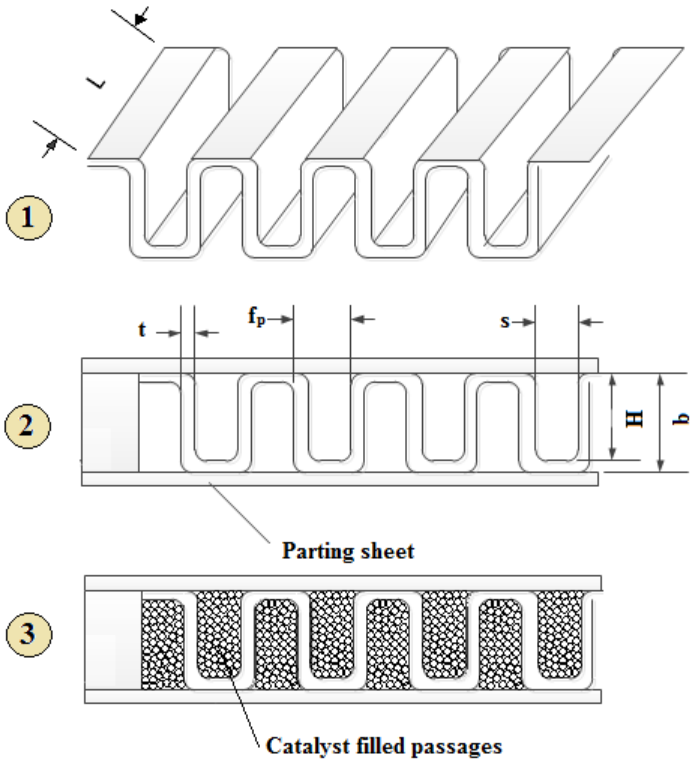

Figure 1: Illustration of the fins (1), and open (2) and catalyst-filled channels (3) within the plate-fin heat exchanger. The geometrical parameters needed to describe the heat transfer coefficients and the friction factors are illustrated in the figure.

2.3. Momentum balances

The momentum balances of all sections can be simplified in terms of differential equations for the pressure

$$\frac{dp_j}{dz} = -f_j \frac{\dot{m}_j{}^2}{2A_j^2\rho_j D_{h,j}}, \tag{6}$$

where p is the pressure, f is the Darcy-Weisbach friction factor factor, A the cross section area, $D_{h,j}$ is the hydraulic diameter of layer j and ρ the density. Both the heat transfer coefficient and the friction factor depended on whether boiling/condensation occurs, if the fluids are single-phase, and if the fluid was in an open channel, or a channel packed with catalyst pellets. Moreover, the mechanisms for transfer of energy and momentum depended on whether the flow was in the laminar or in the turbulent regimes. To take into account the changing conditions in the heat exchanger, heat transfer coefficients and friction factors based on empirical expressions were used, as described in Sec. 2.4

2.4. Heat transfer coefficients and friction factors

2.4.1. The open channels

Heat transfer coefficients and pressure drops vary with pressures, temperatures, compositions, wall temperatures and vapor fractions in the streams. In this work, this was accounted for by using fin specific heat transfer coefficient and friction factor correlations. The heat transfer coefficient for finned geometries

Table 1: The geometrical parameters used to characterize a channel in a plate-fin heat exchanger, where some are illustrated in Fig. 1

Fin type	Plain, Perforated, Serrated
Fin thickness	t
Fin pitch	f_p
Fin height	H
Fin length	L
Fin distance	$s = f_p - t$
Parting sheet distance	$b = H + t$

are typically represented with a j-factor. For serrated fins, the j-factor and friction factor correlations by Manglik and Bergels can be used, where the j-factor correlation reads [21]:

$$j = 0.6522\,\mathrm{Re}^{-0.5403}\left(\frac{s}{H}\right)^{-0.1541}\left(\frac{t}{L}\right)^{0.1499}\left(\frac{t}{s}\right)^{-0.0678}\cdot \left(1 + 5.269\cdot 10^{-5}\,\mathrm{Re}^{1.34}\left(\frac{s}{H}\right)^{0.504}\left(\frac{t}{L}\right)^{0.456}\left(\frac{t}{s}\right)^{-1.055}\right)^{0.1}, \tag{7}$$

which is comprised of dimensionless parameters coming from the fin geometry (see Fig. 1 and Tab. 1) and the Reynolds number, Re. The j-factor is related to the heat transfer coefficient of an open channel through [22]:

$$j = \mathrm{St}\,\mathrm{Pr}^{2/3}, \tag{8}$$

where

$$\mathrm{St} = \frac{\mathrm{Nu}}{\mathrm{RePr}}, \tag{9}$$

and St is the Stanton- , Nu is the Nusselt- and Pr is the Prandtl number, which are dimensionless numbers defined in standard literature on fluid dynamics [22], where the Nusselt number is linear in the heat transfer coefficient. The heat transfer coefficient for rectangular fins can be obtained by using the correlation by Gnielinski, [23] and the friction factor can be obtained by using the correlation by Filonenko [24]. Perforated fins can be treated as plain fins, but with the surface multiplied by a perforation factor of 0.95, meaning that 5% of the area is lost due to perforation, and with the friction factor increased by 20% as recommended by Hesselgreaves [25].

In the two-phase regime, either boiling or condensation occurs, depending on whether the stream is heated or cooled. In this case, the vapor fraction that comes from the enthalpy-pressure flash will be $w_j \in \langle 0, 1\rangle$. The heat transfer in the two-phase regime was decided by the sign on the right-hand-side expression of Eq. 5, i.e. whether $J_{q,j-1,j}$ and $J_{q,j+1,j}$ were positive or negative. If the heat flux is positive, heat enters the channel and boiling is expected to occur. If the heat flux is negative, heat goes out of the channel and the appropriate regime to consider is condensation. The correlation by Bennet and Chen was used for evaporation [26], with the Forster-Zuber correlation for nucleate boiling [27]. The Boyko and Kruhzilin correlation was used for condensation [28]. Since all cases deal with multicomponent mixtures, Silver's [29] and Bell and Ghaly's correlations [30] were used to account for mixture effects in condensation. A transition zone between the two-phase gas/liquid and the single-phase regions had to be used, since some of the correlations diverge when the vapor fraction approaches zero or one. In addition, without smooth transitions, the change of empirical correlations between the two-phase and single-phase areas represents discontinuities. In this work, a linear interpolation between the two-phase and single-phase heat transfer coefficients and friction factors were implemented in the following intervals: $0<w<0.04$, and $0.98<w<1$. Since the Forster-Zuber correlation [27] is a function of the wall temperature, and the wall temperature is a function of the heat transfer coefficient, an algebraic equation had to be solved to obtain the wall temperature in the nucleate boiling regime. The friction factor in the two-phase regime was obtained by using the correlation by Friedel [31].

2.4.2. The catalyst-filled channels

For the layers where catalyst is present, the heat transfer and pressure drop is dominated by the catalyst pellets and the fins contribute in these channels mainly by increasing the available surface area. Following the recommendations by Wesenberg [32], we used the correlation by Peters et al. [33] to describe the wall heat transfer coefficient:

$$\mathrm{Nu}_p = 4.8\left(D_{h,j}/D_p\right)^{0.26}\mathrm{Re}_p^{0.45}\mathrm{Pr}^{1/3}, \tag{10}$$

where we have assumed that the pellets are perfectly spherical, where D_p is the pellet diameter and subscript p for the dimensionless numbers means that the pellet diameter has been used as characteristic length. The pressure drop in the packed channels was calculated by use of the Hicks correlation [34].

2.5. Exergy destruction, entropy production and energy efficiency

Exergy is defined as the maximum theoretical useful work that a system can perform when brought into complete thermodynamic equilibrium with the environment when interacting only with the environment. Exergy destruction or loss of useful work comes from irreversibilities that take place inside the control volume and is related to the total entropy production in the system by the Gouy-Stodola theorem:

$$\dot{E}_\mathrm{d} = T_0\dot{S}_\mathrm{gen}, \tag{11}$$

where $\dot{E}_\mathrm{d}$ is the exergy destruction, also known as the lost work, T_0 is the reference temperature of the environment, taken in this work to be 298 K and $\dot{S}_\mathrm{gen}$ is the total entropy production within the system. In the remaining part of this work, we shall use exergy destruction and lost work interchangeably, where both terminologies refer to the definition provided in Eq. 11.

A significant part of the exergy destruction in the hydrogen liquefaction process is caused by the cryogenic heat exchangers. To increase their efficiency, the exergy destruction and entropy production must be reduced. A first important step in this respect is to identify the origin of the exergy destruction in order to decrease it. This can be accomplished by taking advantage of nonequilibrium thermodynamics to obtain the local exergy destruction [35]. For the plate-fin heat exchanger described in

Sec. 2, the exergy destruction and lost work originate from three contributions:

$$\dot{E}_\mathrm{d} = \dot{E}_T + \dot{E}_P + \dot{E}_{Rx} =$$
$$\int_0^L \left[\underbrace{\sum_1^{n-1} \frac{T_0 \gamma_j J_{q,j+1,j}}{2} \left(\frac{1}{T_j} - \frac{1}{T_{j+1}} \right)}_{\dot{e}_T} \right] dz +$$
$$\int_0^L \left[\underbrace{\sum_1^{n} T_0 A_j v_j \left(-\frac{1}{T_j} \frac{dp_j}{dz} \right)}_{\dot{e}_P} \right] dz + \qquad (12)$$
$$\int_0^L \left[\underbrace{\sum_1^{n} T_0 r_{o\to p} \left(-\frac{\Delta G_{o\to p,j}}{T_j} \right)}_{\dot{e}_{Rx}} \right] dz,$$

where n is the total number of layers, $\Delta G_{o\to p,j}$ is the Gibbs free energy of the ortho-para hydrogen conversion in layer j, $\dot{E}_T$, $\dot{E}_P$ and $\dot{E}_{Rx}$ represent the total exergy destruction within the heat exchanger from heat transfer, pressure drop and ortho-para hydrogen conversion respectively. Analogously, $\dot{e}_T$, $\dot{e}_P$ and $\dot{e}_{Rx}$ represent the local exergy destruction within the heat exchanger, with units of [W/m]. Note that for the layers where no ortho-para hydrogen conversion takes place, $r_{o\to p} = 0$ and the last term on the right-hand-side of Eq. 12 is zero. The local entropy production that was used to compute the local exergy destruction in Eq. 12 can be derived similarly as in Ref. [36]. By analyzing the different terms in Eq. 12, we shall identify the main sources and the location of the exergy destruction within the cryogenic heat exchanger and explore strategies to decrease it.

3. Cases

The typical hydrogen liquefaction process has four consecutive stages as elaborated in Sec. 1. In this work, we shall study a heat exchanger in the cryogenic cooling stage (Stage 3). Three main cases will be considered.

The purpose of the heat exchangers investigated in this work is to cool reacting and non-reacting streams (where no catalyst is present) of hydrogen from 47.8 K to a target temperature for the reacting hydrogen of below 29.3 K. The non-reacting stream in the heat exchanger model represents the Joule–Thomson branch of a Claude-type hydrogen liquefaction process. The inlet pressure of both hot hydrogen streams was set to 1.96 MPa. The total flow rate of reacting and non-reacting hydrogen were 50 tons/day and 21.4 tons/day respectively. The cold-side refrigerant inlet temperature was 28.9 K in all cases, where the refrigerant flow rate was adjusted to match the desired outlet temperature of the reacting hydrogen (below 29.3 K). To be able to compare the cases, the geometry of the heat exchanger was fixed according to the parameters in Tab. 2 with alternating hot and cold layers, where the two hot streams were allocated

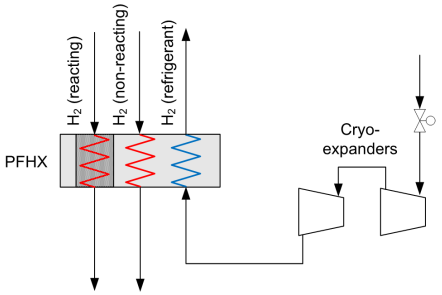

(a) The Reference Case

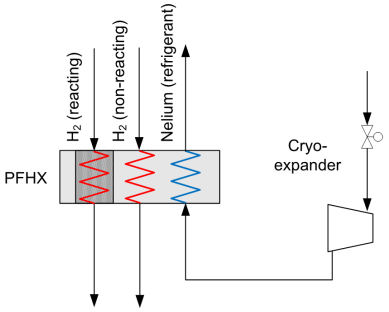

(b) The Nelium Case

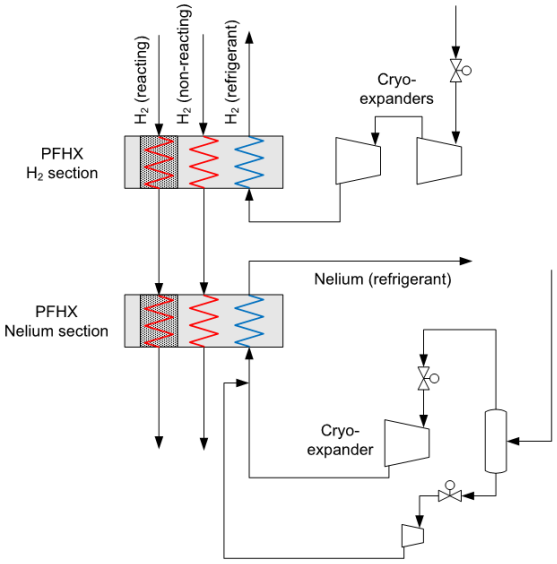

(c) The Hybrid Case

Figure 2: An illustration of the different heat exchanger configurations discussed in this work. The dark-shaded areas represent layers with catalyst.

to equal number of layers in the plate-fin heat exchanger. The hot and cold-streams flowed counter-currently through the heat exchanger. The geometry of the plate-fin heat exchanger, summarized in Tab. 2, was found by using typical temperatures, pressures and flow rates of a hydrogen Claude process and adjusting the geometry until a reasonable mean temperature difference was achieved (below 2 K). Three main cases, illustrated in Fig. 2, will be studied in this work:

The Reference Case: This case considers a heat exchanger in the bottom part of a Claude hydrogen liquefaction process, as depicted in Fig. 2a. Before final expansion, the reacting hydrogen stream is very close to the Joule–Thomson inversion line. The refrigerant stream in this case is gaseous hydrogen expanded through cryo-expanders. The inlet pressure for the cold-side hydrogen refrigerant was set to 0.5 MPa.

The Nelium Case: This case is similar to the Reference Case, except that a mixture with 90 mole percent neon and 10 mole percent helium (Nelium-90) was used as refrigerant, as depicted in Fig. 2b. The inlet pressure for the Nelium was set to 1.0 MPa, where the refrigerant entered the heat exchanger in the two-phase regime.

The Hybrid Case: This case represents a mix of the previous two configurations, where hydrogen was used as refrigerant at high temperatures ($z < 1.0$ m), and Nelium-90 was used at low temperatures ($z \geq 1.0$). A possible process configuration for this case is illustrated in Fig. 2c.

For simplicity, without affecting results or conclusions principally, the return stream of non-reacting hydrogen was omitted from the heat exchanger simulations for all the cases considered. The para-hydrogen mole fraction at the inlet of the reacting hydrogen stream was set to be 3 mole-percentages below its equilibrium-composition, i.e., $x_{H_2,\mathrm{p}}(z = 0) = 0.767$. In addition to the three main cases above, we shall also consider a sub-case called "improved catalyst - IC":

The Improved Catalyst (IC) sub-cases: In this case, all parameters were kept the same as in the respective main cases, except that the reaction rate in Eq. 3 was multiplied by a factor of 2. This was done to emulate a doubling of the catalytic activity in comparison to ferric-oxide catalyst. According to Hutchinson and coworkers [12], nickel oxide-silica catalyst has displayed activities on a volumetric basis that are twice as high as ferric-oxide catalyst.

4. Results

We evaluate first the accuracy of key submodels employed (Sec. 4.1). Cases are discussed in 4.2, before strategies to reduce the exergy destruction in the plate-fin heat exchanger are evaluated in Sec. 4.3.

Table 2: Parameters that characterize the geometry of the plate-fin heat exchanger. See Fig. 1 and Tab. 1 for explanation and illustration of the parameters.

Parameter	Value	Units
Type	Regular	
Length	2	m
Width	1.5	m
Height	0.8	m
Fin height	4	mm
Fin thickness	0.35	mm
Fin Spacing	1.1	mm
Parting sheet distance	1.5	mm

4.1. Evaluating the accuracy of the submodels

4.1.1. Modeling the phase equilibrium of Nelium

While the equations of state for ortho and para hydrogen presented by Leachman et al. [2] have high accuracies, no high-accuracy EoS is currently available for the helium-neon mixture. Heck and Barrick [37] and Knorn [38] measured in 1967 phase-equilibrium compositions of the helium-neon mixture at various conditions. We used these experimental data to find the interaction coefficient, k_{ij}, of the cubic Peng Robison EoS by minimizing the mean square deviation with respect to the experimental data. The optimal value when using the conventional van der Waals mixing rule was found to be, $k_{ij} = 0.15$.

A comparison between the Peng Robinson EoS and the experimental data are displayed in Fig. 3. The figure shows that the EoS reproduces dew points significantly better than bubble points, and that there is a considerable potential for improvement. We tested several other EoS such as Peng Robinson with Huron-Vidal mixing rules and SPUNG (see Ref. [39] for details about these models), but the improvement in comparison to the Peng Robinson EoS was very modest. We therefore decided to use the Peng Robinson EoS to describe mixtures of helium and neon in this work.

Figure 3 shows that the Peng Robinson EoS captures the phase behavior of the helium-neon mixture reasonably well from a qualitative perspective, but that a more accurate EoS for the helium-neon mixture should be developed in the future. New experimental data of higher accuracy are probably needed to achieve this.

4.1.2. Modeling the ortho-para conversion

Hutchinson and coworkers presented both experimental data and theoretical models for the reaction rate of the ortho-para hydrogen conversion in the presence of 30–50 mesh sized ferric oxide catalyst [12–14]. Measurements were also carried out by Weitzel and coworkers [15] at different conditions. Hutchinson et al. [12] stated that Eq. 3 was capable of representing the experimental data to a reasonable accuracy. Unfortunately, no fitted expressions for the empirical parameters n and K were presented. The experimental data available in the literature are typically represented as outlet mole fractions of para hydrogen

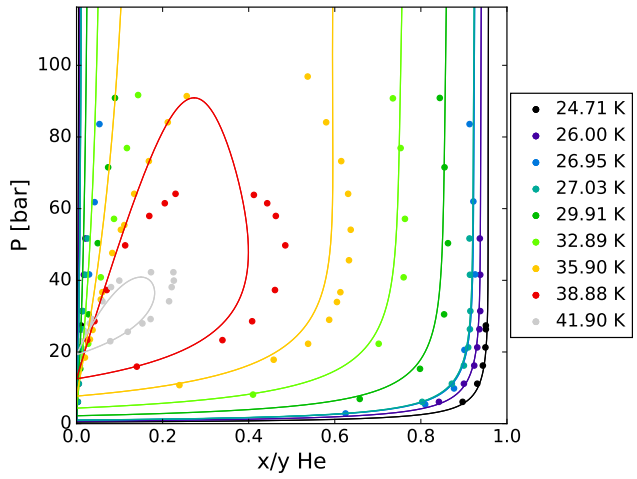

Figure 3: A pressure-composition plot of the vapor–liquid compositions (bullets) and the Peng Robinson EoS (solid lines) with $k_{ij} = 0.15$ at various temperatures (indicated by colors). Here, x represents the mole fraction in the liquid-phase and y the mole fraction in the vapor-phase.

as functions of the space velocity in the experimental facility:

$$v_s = \frac{\dot{V}_{H_2,p}}{V}, \tag{13}$$

where $\dot{V}_{H_2,p}$ is the volumetric flow rate at the inlet, and V is the total volume of the reactor. Hutchinson and coworkers stated that n should be a positive function of T and that K should be a function of both T and P. We solved Eq. 2 with Eq. 3 as input at isothermal conditions to a relative accuracy of 10^{-5}, where we used different mathematical expressions for K and n as functions of temperature and pressure, following the guidelines suggested by Hutchinson et al. [12]

For each mathematical expression, we performed several unconstrained nonlinear optimizations at different initial conditions to identify the choice of parameters that minimized the mean square deviation between predictions from the kinetic model and a total number of 997 experimental measurements for 30–50 mesh sized ferric oxide catalyst (see Tab. 4 for details). We evaluated a wide range of expressions with different number of fitting parameters, however, we found that little improvement could be achieved beyond 4 parameters, where n and K were found to be captured well by the following expressions:

$$n = a, \tag{14}$$

$$K = b + c\tau + d\varrho. \tag{15}$$

Here, $\tau = T/T_c$ and $\varrho = P/P_c$ where T_c and P_c are the critical temperature and pressure of normal hydrogen and a, b, c, d are parameters. All parameters are provided in Tab. 3.

The average deviation between the measured and calculated outlet molar fractions of para hydrogen was 2.2% with 4 parameters and a very modest improvement to 2.0% could be achieved by using as many as 9 parameters, where we in the 9-parameter expression included all second order combinations between τ and ϱ and a second order temperature dependence for n. The lower number of parameters were chosen as there is risk of actually fitting systematic experimental error when using an unnecessary large number of coefficients, in particular when the improvement is small. Moreover, the simpler expressions are expected to extrapolate better outside of the regime where experimental data are available. Table 3 shows that the kinetic model can be used to obtain the reaction rates in the temperature range 23 K–86 K and for pressures up to 7.0 MPa with an average deviation of 2.2% and a maximum deviation of 14.3%.

Figures 4 and 5 show that the expression in Eq. 15 with parameters in Tab. 3 (solid lines) captures the trend in experimental data by Hutchinson and coworkers [13, 14] very accurately at several temperatures and pressures, both for the backward reaction in Eq. 1 (Fig. 4), and for the forward and backward ortho-para hydrogen conversion at 77 K (Fig. 5). The data by Weitzel et al. are also represented to a reasonable accuracy, however they are represented less accurately than the data by Hutchinson, as is evident from Fig. 6 and Tab. 4. Even tough the same catalyst has been used, the outlet molar fractions of para hydrogen from the experiments by Weitzel et al. appear to be more linear as functions of space velocity than the molar fractions from Hutchinson's work. This may be attributed to experimental uncertainty or a difference in the experimental procedures. Nonetheless, it is clear that Eq. 15 with the parameters from Tab. 3 captures the available experimental data reasonably well.

Table 3: The parameters used in the expression for the ortho-para conversion reaction rate in Eq. 15. The critical parameters were obtained from Ref. [2]

parameter	value	unit
T_c	32.937	K
P_c	1.28377	MPa
a	1.0924	-
b	0.0597	kmol/m^{3}s
c	-0.2539	kmol/m^{3}s
d	-0.0116	kmol/m^{3}s

Since the experiments on ferric oxide catalyst for catalyzing the ortho-para conversion were carried out in the 1960s, a natural question to ask is whether the correlation developed in the present work applies to state-of-the-art catalysts. In fact, the same ferric oxide catalyst is available commercially today, with the registered trade name IONEX catalyst. The supplier of IONEX catalyst guarantees a conversion to 46.5% of para hydrogen at $v_s = 1200$ per min at standard temperature and pressure (STP), 77K and 1.36 bar. Figure 7 shows the predicted outlet molar fractions of para hydrogen from the kinetic rate correlation developed in this work (solid line), which lies well above the outlet molar fraction guaranteed by the supplier (red cross). Hence, the reaction rate predicted by the correlation presented in this work should be representative of the reaction rate of the ferric oxide catalyst that is available commercially today.

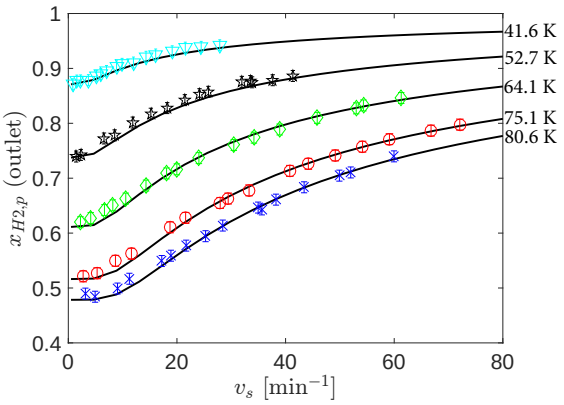

(a) P = 2.84 MPa

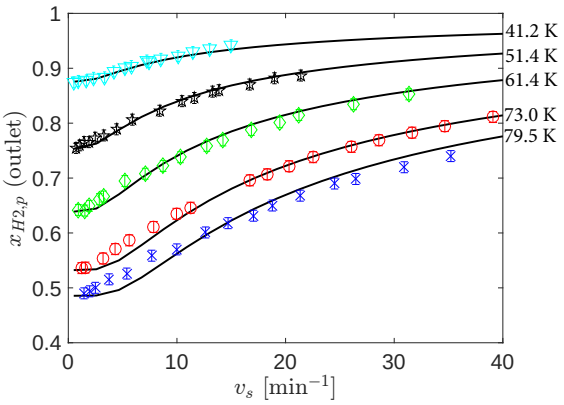

(b) P = 5.60 MPa

Figure 4: Conversion of para to ortho hydrogen as a function of the space velocity. The markers represent experiments from Ref. [13] at two different pressures (a/b) and different temperatures: Cyan triangles 41.6/41.2 K, black stars 52.7/51.4 K, green diamonds 64.1/61.4 K, red circles 75.1/73.0 K, blue crosses 80.6/79.5 K.

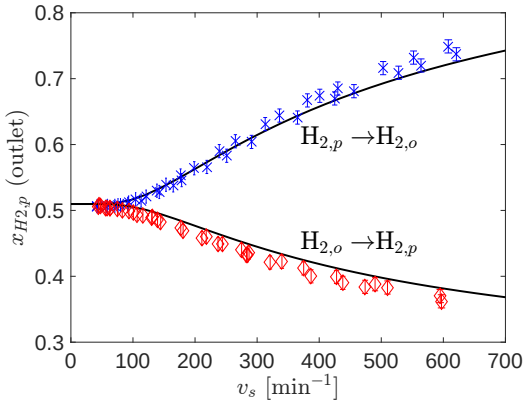

(a) P = 0.21 MPa

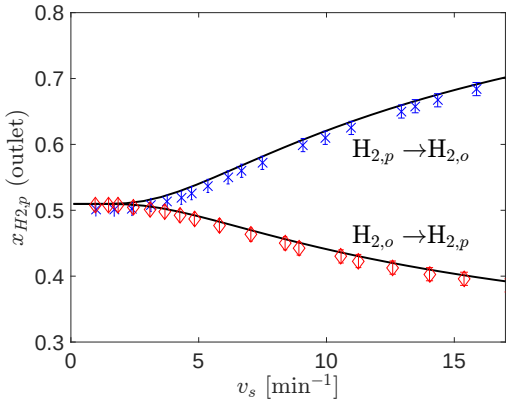

(b) P = 6.96 MPa

Figure 5: Forward and backward conversion of ortho- and para hydrogen as a function of the space velocity. The markers represent experiments from Ref. [13] at 77 K at two different inlet mole fractions of para-hydrogen of 0.99 (blue crosses) and 0.25 (red diamond markers).

Table 4: The deviation between experimental data and the reaction rate expression in Eq. 15 with parameters from Tab. 3

Reference	[13]	[14]	[15]	All
Number of Exp.	471	256	270	997
Direction of Eq. 1	←	→	→	both
T-span [K]	41.3–82.7	76	23.4–85.6	23.4–85.6
P-span [MPa]	0.3–7.0	0.2–7.0	2.2	0.2–7.0
Mean deviation [%]	1.5	2.3	3.2	2.2
Max deviation [%]	8.5	8.7	14.3	14.3

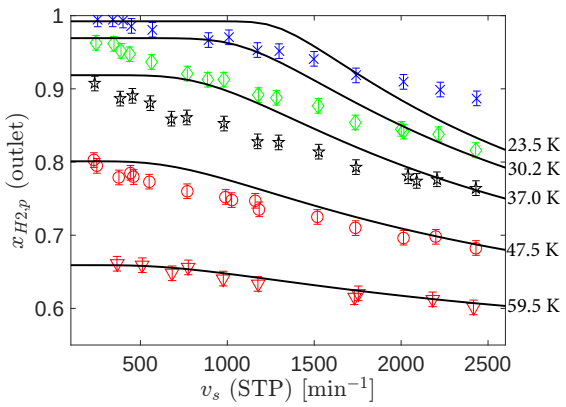

Figure 6: Conversion of para to ortho hydrogen as a function of the space velocity at different temperatures with an inlet mole fraction of para hydrogen of 0.515 at a pressure of 0.14 MPa [15]. The following temperatures are presented: blue crosses 23.5 K, green squares 30.2 K, black stars 37 K, red circles 47.5 K, red triangles 59.5 K.

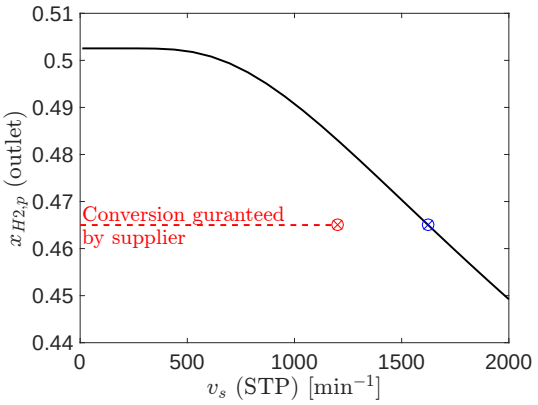

Figure 7: Conversion of para to ortho hydrogen as a function of the space velocity at 77K and 1.36 bar predicted by the kinetic model (solid line). The red point shows the conversion guaranteed by the supplier of the IONEX catalyst. The kinetic model predicts that the conversion guaranteed by the supplier is obtained with good margin (compare the red cross with the blue cross).

4.2. A comparison of the cases

A total of six cases have been investigated, where details can be found in Sec. 3. Key parameters such as outlet para hydrogen mole fractions and refrigerant flow rates are displayed in Tab. 5. The inlet molar fraction of para hydrogen was in all cases set to 0.767, and the outlet molar fractions of para hydrogen were similar for all the cases that had the same catalyst, varying between 0.935 and 0.938 for the cases with standard catalyst and between 0.962 and 0.969 for the cases with improved catalyst. However, we shall see in Sec. 4.3 that the difference in exergy destruction due to the ortho-para reaction is much more significant than what the outlet molar fraction of para hydrogen indicates.

Figure 8 shows the temperature profiles through plate-fin heat exchangers with total lengths of 2.0 m. The refrigerant flow rate of the Nelium case was adjusted to achieve as small temperature difference between the hot and cold layers as possible, since all realistic flow rates yielded temperatures below the reference case (29.3 K), as shown in Tab. 5. The temperatures are shown as functions of both the accumulated heat transferred between the hot and cold streams, Q, in terms of composite curves (Figs. 8a,8c,8e) and as functions of position (Figs. 8b,8d,8f). The Reference case, where normal hydrogen is used as refrigerant is displayed in Figs. 8b and 8a. The figures show a relatively constant temperature difference until a location of $z = 1.2$ m, where the difference in temperature between the cold and hot streams of the heat exchanger starts to increase. The figure shows that at temperatures below about 40 K, the thermal match between the reacting mixture and the hydrogen refrigerant starts to decay. The reason for this is a large positive peak in the heat capacity of the hot-side hydrogen (1.96 MPa) at this location, while the heat capacity of the hydrogen refrigerant (0.5 MPa) has no peak.

In the Nelium case, a mixture of helium and neon boils in the cold layers of the plate-fin heat exchanger. This increases the overall heat transfer coefficient significantly in comparison to single-phase heat transfer, in particular with the layers filled with catalyst that have a heat transfer coefficient that is approximately 60 times larger than that of the open layers. The correlations described in Sec. 2 predict that the overall heat transfer coefficient between the cold layers and the catalyst filled layers increases nearly 40 times when Nelium boils. This explains the tight thermal match between the cold and the hot side in the Nelium case at the location 1 m $< z <$ 2 m. At $z = 0.55$ m however, the Nelium has become superheated vapor, and the overall heat transfer coefficient drops. This gives a poor thermal match in the Nelium case at this location, where the temperature difference reaches a magnitude of 6.2 K. The reason for the rapid increase in the temperature of the Nelium stream at $z < 0.55$ m, is that all the transferred heat is then used to heat the gaseous refrigerant, because all the liquid has boiled off. Before that point, a significant part of the heat transferred from the hot streams is used to evaporate the neon-rich liquid-phase. A comparison of Figs. 8c and 8d elucidates that even if the large temperature gradients between the hot and the cold streams occurs in only a relatively small part of the heat exchanger ($z < 0.55$ m), almost 50% of the overall heat is transferred here.

It is clear from Figs. 8c and 8d that Nelium enables a tight thermal match in the end region of the heat exchanger, at temperatures below 40 K. A natural next step is therefore to combine the two refrigerants in two separate heat exchangers, as in the Hydrogen-Nelium Hybrid case (see Fig. 2c). Figures 8e and 8f show that the Hybrid case has a smaller temperature difference between the hot and cold layers than the two other cases.

4.3. Evaluating strategies to reduce the entropy production and exergy destruction in the heat exchangers

Table 6 reveals that the two main sources of exergy destruction in the plate-fin heat exchangers are temperature gradients (Term 1 on the right-hand-side of Eq. 12) and conversion of ortho to para hydrogen (Term 3 on the right-hand-side of Eq. 12), being responsible for 69% and 29% of the exergy destruction in the Reference case respectively. The exergy lost due to a pressure-drop in the heat exchanger is 2.7% (Term 2 on the right-hand-side of Eq. 12). Similar to previous work [36], a correct implementation and computation of the terms in Eq. 12 was ensured by calculating the total entropy production from an overall entropy balance and confirming that it was equal to the sum of the integrals on the right-hand-side of Eq. 12 within the numerical accuracy of the calculations.

The large exergy destruction from the ortho-para hydrogen conversion can be understood on the basis of Fig. 9a, where the para-hydrogen mole fraction of the Reference case differs between 3.0–8.3 mole percent from the equilibrium mole fraction through the heat exchanger (blue dashed line). This translates into a high negative value for the Gibbs energy, $\Delta G_{o\rightarrow p}$, and significant amount of exergy destruction in the layers packed with catalyst. Even though the superficial gas velocity within the packed bed of the plate-fin heat exchanger is low (0.65 m/s), the ortho-para mixture is still far away from the ortho-para equilibrium state due to slow reaction kinetics. Note that the exergy destruction from the ortho-para hydrogen conversion will not be captured by overall process simulations that assume that the

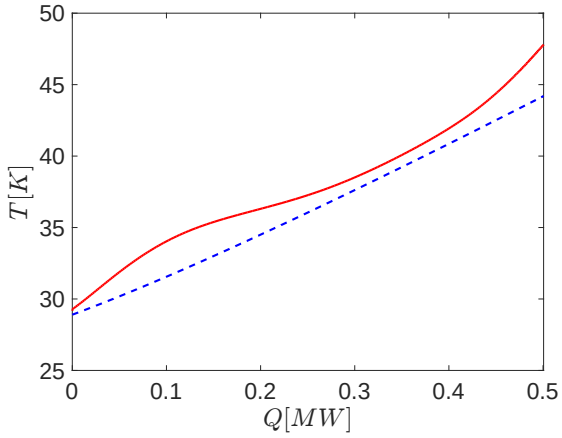

(a) The reference case

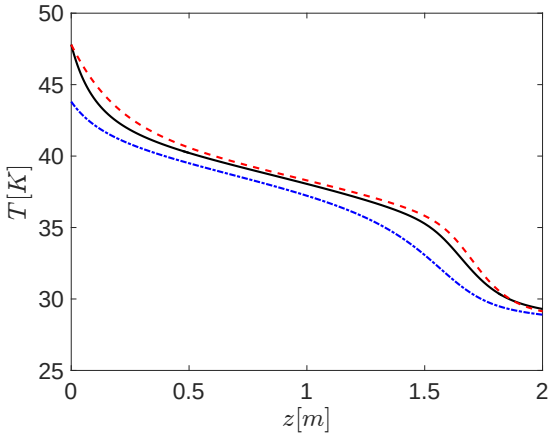

(b) The reference case

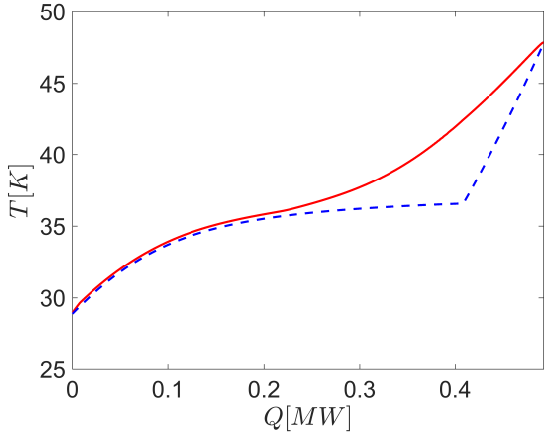

(c) The Nelium case

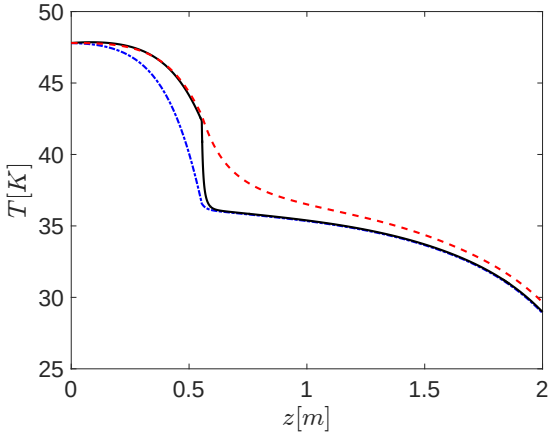

(d) The Nelium case

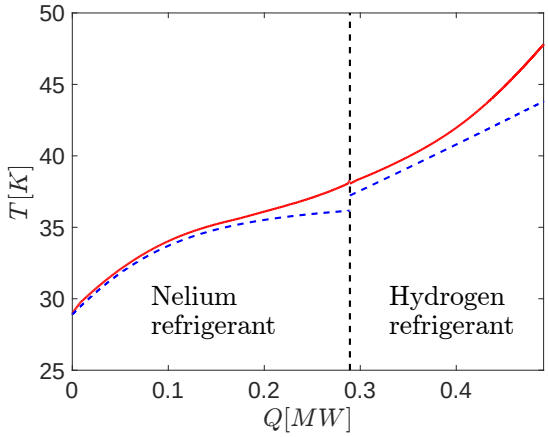

(e) The Hybrid case

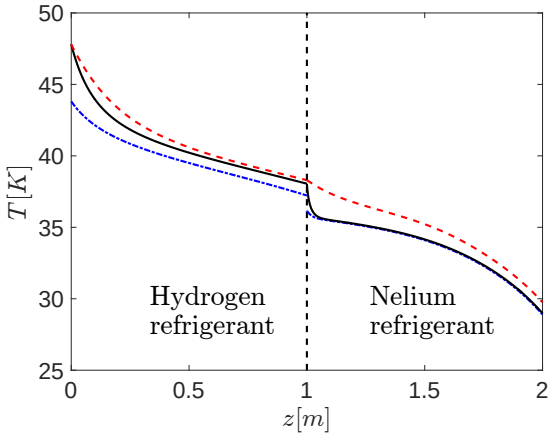

(f) The Hybrid case

Figure 8: The subfigures on the left-hand-side show composite curves of the hot streams (red solid lines) and cold streams (blue dashed lines) where the temperatures of the hot (red solid lines) and cold layers (blue dashed lines) are plotted as functions of the accumulated amount of heat transferred, Q. The subfigures on the right-hand-side show temperatures of the reacting mixture (solid line), the refrigerant (blue dash-dot line) and the non-reacting hydrogen stream (red dashed line) as functions of position through the heat exchanger

Table 5: Key results from the cases investigated. IC: Improved Catalyst, means that the reaction rate in Eq. 3 has been doubled. Here, $\dot{F}$ is the molar flow rate.

Cases	F_{H2} [kmol/s]	F_{Ne} [kmol/s]	$T_{\text{out,h2,p}}(z = L)$ [K]	$x_{\text{out,h2,p}}(z = L)$
Reference	1.29	0.00	29.3	0.935
Reference - IC	1.29	0.00	29.3	0.962
Nelium	0.00	0.27	29.0	0.938
Nelium - IC	1.29	0.28	28.9	0.969
Hydrogen - Nelium hybrid	1.29	0.27	29.0	0.937
Hydrogen - Nelium hybrid - IC	0.00	0.28	29.0	0.964

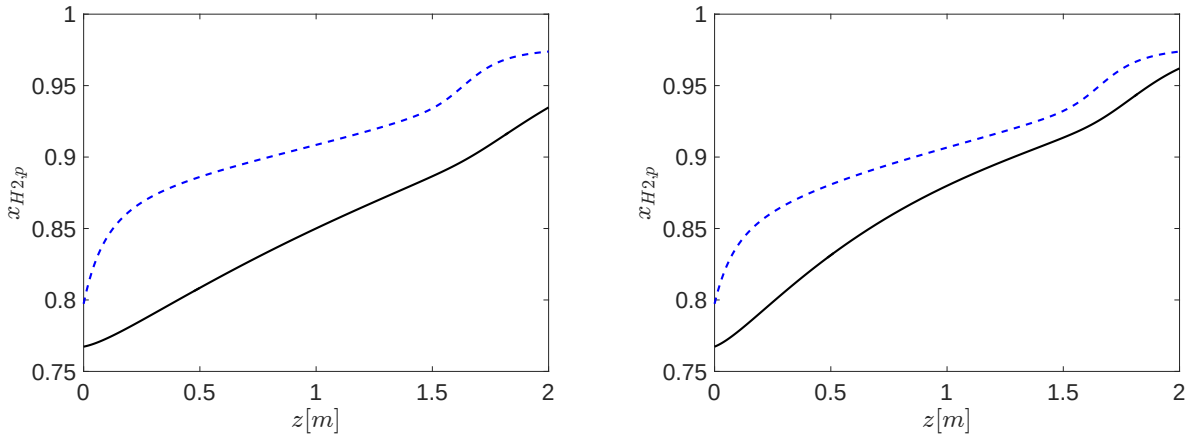

(a) Reference case

(b) Reference case with improved catalyst

Figure 9: The mole fraction of para-hydrogen through the heat exchanger (solid line), the equilibrium value (blue dashed line) for the Reference case (a) and for the Reference case with improved catalyst (b)

reacting mixture is all the time at equilibrium [5–9, 40], and detailed unit modeling is crucial to account for these losses.

The best remedy to reduce the exergy destruction from the ortho-para hydrogen conversion is to develop more efficient catalyst which leads to a higher reaction rate, $r_{\text{o}\to\text{p}}$ and a mixture that is closer to equilibrium through the heat exchanger. Alternatively, the residence time can be increased by constructing a larger heat exchanger and lowering the flow rate through each layer. The maximum block-size of the heat exchanger will, however, limit the potential reduction that can be achieved by this route.

According to discussions by Hutchinson and coworkers [12], nickel oxide-silica catalyst has displayed activities on a volumetric basis that are twice as high as ferric-oxide catalyst. We solved the Reference case with the reaction rate multiplied by a factor two to emulate nickel oxide-silica catalyst, assuming otherwise that the reaction mechanism follows the same steps. The results are reported in the row entitled "Reference case - Improved Catalyst (IC)" in Tab. 6. A doubling of the reaction rate reduces the exergy destruction due to reaction, $\dot{E}_{Rx}$, by 35% and the overall exergy destruction by 9%. The reaction is closer to equilibrium through the heat exchanger in the IC-Case, as is evident by comparing Figs. 9a and 9b. A mole fraction of para hydrogen that is closer to its equilibrium value at the corresponding temperature of the stream translates into a smaller value for $\Delta G_{o\to p}$ and hence a lower exergy destruction. The results summarized in Tab. 6 indicate that there is a maximum potential to reduce the exergy destruction in the heat exchanger of 29%. This potential can be approached by developing more efficient catalyst for the ortho-para conversion.

The largest source of exergy destruction and lost work in the plate-fin heat exchanger is the temperature difference between the hot and cold layers shown in Fig. 8. Since the exergy destruction is proportional to ΔT^{-1}, a heat transfer process at 30 K gives an exergy destruction that is about one hundred times larger than at atmospheric conditions with the same heat flux and temperature difference. Thermal exergy destruction is therefore particularly parasitic in the cryogenic part of the hydrogen liquefaction process. To mitigate these losses, it is necessary to reduce the temperature difference between the layers. A possible avenue to achieve this is by increasing the overall heat transfer coefficient, e.g. by using evaporating refrigerant on the cold-side of the heat exchanger. The helium-neon mixtures represents a possible refrigerant for this purpose. In this work, we have used a mixture with 90 mole-% neon and 10 mole-% helium in order to have a refrigerant that evaporates over the appropriate temperature range.

Fig. 10 presents graphical representations of where the work is lost locally through the heat exchangers. Here, the dark-shaded area represents thermal exergy destruction and the yellow area represents exergy destruction from the ortho-para-hydrogen conversion. The most evident characteristic of these

Table 6: Exergy destruction/ Work lost in the heat exchangers in the different cases investigated. Here, IC: Improved Catalyst means that the reaction rate in Eq. 3 has been multiplied by a factor of two.

Cases	$\dot{E}_{Rx}$ [kWh/kg H_2]	$\dot{E}_T$ [kWh/kg H_2]	$\dot{E}_P$ [kWh/kg H_2]	$\dot{E}_d$ [kWh/kg H_2]	Percent deviation
Reference	0.036	0.088	$3.5{\cdot}10^{-3}$	0.128	0.0
Reference - IC	0.024	0.088	$3.6{\cdot}10^{-3}$	0.116	-9.4
Nelium	0.046	0.071	$2.3{\cdot}10^{-3}$	0.119	-7.0
Nelium - IC	0.036	0.074	$2.1{\cdot}10^{-3}$	0.112	-12.2
Hydrogen - Nelium hybrid	0.036	0.044	$2.2{\cdot}10^{-3}$	0.083	-34.9
Hydrogen - Nelium hybrid - IC	0.024	0.046	$2.3{\cdot}10^{-3}$	0.072	-43.2

figures is the spikes found in the profiles. For the reference case, a spike in the local exergy destruction is located at about $z = 1.5$ m, as well as at the hot inlet of the heat exchanger ($z = 0$). Figure 8b shows that the location of the spikes corresponds to the locations where the temperature difference between the hot and the cold streams are highest. The exergy destruction from the ortho-para conversion (yellow shaded area), seems to be largest after the spikes, when the temperature of the reacting hydrogen has changed by a large amount in a short distance.

Fig. 10b shows that a spike in the local exergy destruction can also be found in the Nelium case at the location $z = 0.55$ m. This spike is more than three times larger in magnitude than the largest spike of the Reference case. Except at $z = 0.55$ m, the local exergy destruction is significantly smaller in the Nelium case than in the Reference case due to the increase in the overall heat transfer coefficient. However, the large magnitude of the spike in the local exergy destruction causes the overall exergy destruction in the Nelium case (0.119 kWh/kg H_2) to be only 7.0 % lower than the exergy destruction in the reference case (0.128 kWh/kg H_2), as shown in the last column of Tab. 6. From an overall process point of view, the use of Nelium as refrigerant is also beneficial for the energy efficiency since it enables the use of efficient and scalable compressor and expansion equipment (see the discussion in Sec. 1).

Since the reference case has its largest exergy destruction at the cold end of the heat exchanger ($z = L$), and the Nelium case has the largest exergy destruction at the hot end ($z = 0$), a route to reduce the exergy destruction in the plate-fin heat exchanger is to make a process configuration that combines these refrigerants, as described in section 4.2. In the Hydrogen-Nelium Hybrid case, hydrogen has been used as refrigerant in the first half of the heat exchanger ($z < 1.0$), after which the Nelium-90 mixture was used as refrigerant. The same flow rates were used as in the Reference and Nelium cases. Figure 10c shows the local exergy destruction in the Hybrid case, which displays a spike at the hot inlet ($z = 0$ m) and at the hot inlet of the second heat exchanger ($z = 1.0$ m). The enhanced heat transfer in the second heat exchanger leads to a 34.9% decrease of the exergy destruction in the heat exchanger (0.083 kWh/kg H_2). Nelium has thus an unrealized potential as refrigerant in the bottom part of the hydrogen liquefaction process. However, Nelium is arguably most attractive as refrigerant for hydrogen temperatures below 40 K, since it may then be used as refrigerant in the two-phase regime, which gives enhanced heat transfer and a lower exergy destruction.

If improved catalyst is used in combination with a hybrid refrigerant strategy, it is possible to reduce the energy losses in the heat exchanger by 43.2%, as shown in the last row of Tab. 6. Note that no optimization of geometry, refrigerant composition or pressures has been carried out in this work, as this will be closely connected to the characteristics of the overall process. However, it is clear that there are at least two viable routes to significantly reduce the exergy destruction in plate-fin heat exchangers in the bottom part of the hydrogen liquefaction process: (1) Develop more efficient catalyst and (2) Use a boiling mixture, e.g. of Nelium as refrigerant at temperatures below 40 K. Its composition can be tailored to give a tight thermal match. Optimization of temperatures, pressures and refrigerant compositions and heat exchanger geometry in combination with an overall process simulation that uses a detailed heat exchanger model should be carried-out in future work to further evaluate and improve these strategies.

5. Conclusion

In this work, we have discussed strategies to reduce the exergy destruction and lost work in the plate-fin heat exchangers in the cryogenic part of a hydrogen liquefaction process. For this purpose, we developed a detailed model of a plate-fin heat exchanger, incorporating the geometry, nonequilibrium ortho-para conversion and correlations to account for the pressure drop and heat transfer coefficients due to possible boiling/condensation of the refrigerant at the lowest temperatures. Based on available experimental data, a correlation for the ortho-para conversion kinetics was developed, that reproduced the available experimental data with an average deviation of 2.2%.

In a plate-fin heat exchanger that cools the hydrogen from 47.8 K to 29.3 K by use of hydrogen as refrigerant, we found that the total amount of exergy destruction was 0.128 kWh/kg H_2. There were two main sources of exergy destruction; the temperature difference between the hot and cold layers and the ortho-para hydrogen conversion, being responsible for 69% and 29% of the exergy destruction respectively. Several heat exchanger cases were considered; a reference case with hydro-

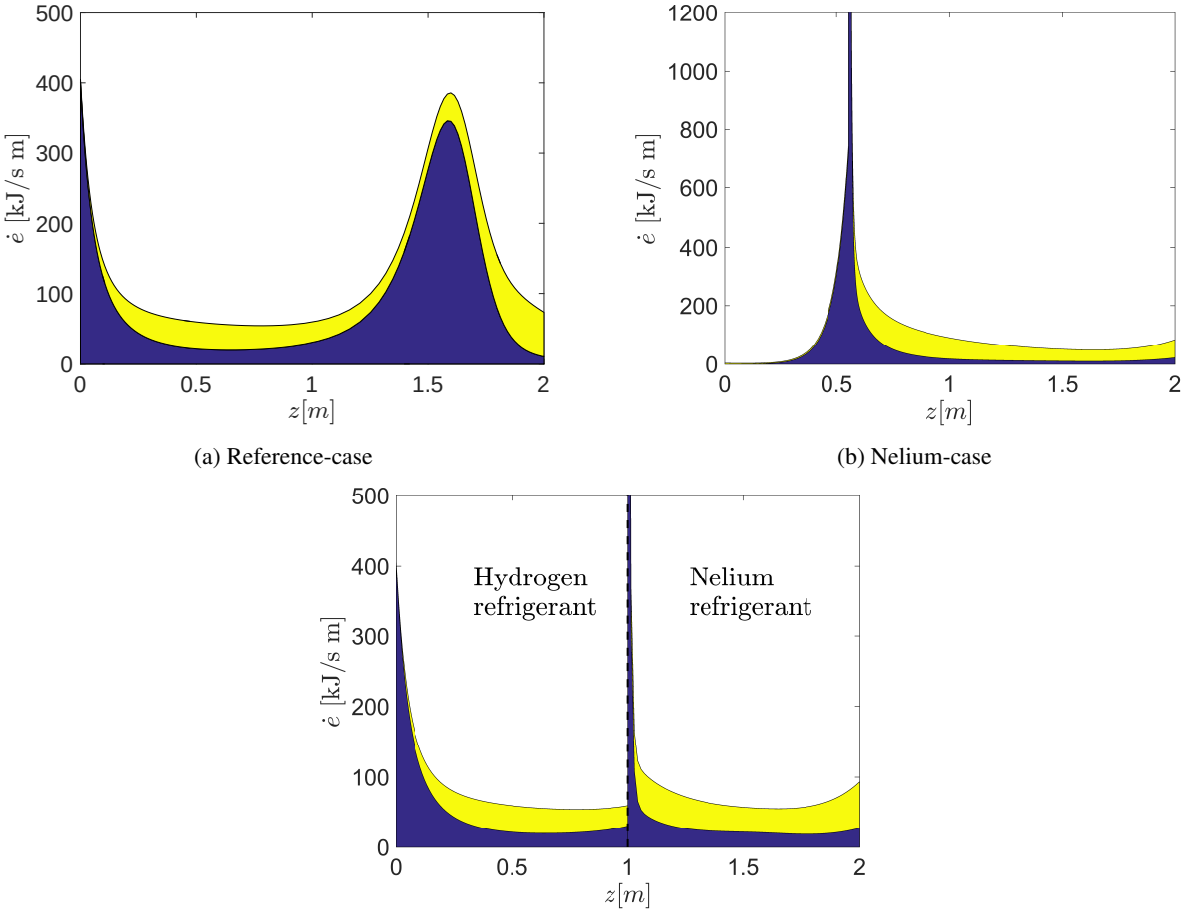

(a) Reference-case

(b) Nelium-case

(c) Hybrid-case

Figure 10: The local exergy destruction/lost work through the heat exchanger. Here the blue shaded area represents the thermal exergy destruction, and the yellow shaded area is the exergy destruction from the ortho-para conversion.

gen as refrigerant, a novel case where a helium-neon (Nelium) mixture was used as refrigerant and a hybrid case where both hydrogen and Nelium were used as refrigerants in two heat exchangers connected in series.

It was found that a viable route to reduce the exergy destruction from the ortho-para hydrogen conversion was to use a more efficient catalyst, where a doubling of the catalytic activity in comparison to ferric-oxide, as demonstrated by nickel oxide-silica catalyst, reduced the overall exergy destruction by 9%. A route to reduce the thermal losses was to employ an evaporating Nelium mixture at the cold-side of the heat exchanger, which reduced the overall exergy destruction by 7%. This was a particularly attractive solution at hydrogen temperatures below 40 K, since a thermal mismatch occurred when the Nelium changed from the two-phase to the single-phase regime at the cold side of the heat exchanger.

It was found that a combination of using hydrogen and Nelium as refrigerants enabled a reduction of the exergy destruction by 35%. Moreover, a combination of improved catalyst and the use of hydrogen and Nelium as refrigerants reduced exergy destruction in the cryogenic heat exchangers by 43%.

We have in this work presented and evaluated two viable strategies to reduce the entropy production, exergy destruction in the plate-fin heat exchangers in the cryogenic part of the hydrogen liquefaction process. Further optimization of temperatures, pressures and refrigerant compositions in combination with an overall process simulation that uses a detailed heat exchanger model should be carried-out to further evaluate these strategies. We find that the limited efficiency of the ortho-para catalyst represents a barrier for further improvement of the efficiency, and future research should address this.

Acknowledgment

This publication is based on results from the research project Hyper, performed under the ENERGIX programme. The authors acknowledge the following parties for financial support: Statoil, Shell, Kawasaki Heavy Industries, Linde Kryotechnik, Mitsubishi Corporation, Nel Hydrogen and the Research Council of Norway (255107/E20).

References

[1] M. Voldsund, K. Jordal, R. Anantharaman, Hydrogen production with CO_2 capture, International Journal of Hydrogen Energy 41 (9) (2016) 4969–4992. doi:10.1016/j.ijhydene.2016.01.009.

[2] J. W. Leachman, R. T. Jacobsen, S. G. Penoncello, E. W. Lemmon, Fundamental equations of state for parahydrogen, normal hydrogen, and orthohydrogen, Journal of Physical and Chemical Reference Data 38 (2009) 721. doi:10.1063/1.3160306.

[3] O. Burheim, Engineering energy storage, Elsevier, London, United Kingdom, 2017.

[4] D. Berstad, J. H. Stang, P. Nekså, Comparison criteria for large-scale hydrogen liquefaction processes, International Journal of Hydrogen Energy 34 (3) (2009) 1560–1568. doi:10.1016/j.ijhydene.2008.11.058.

[5] D. Berstad, J. H. Stang, P. Nekså, Large-scale hydrogen liquefier utilising mixed-refrigerant pre-cooling, International Journal of Hydrogen Energy 35 (10) (2010) 4512–4523. doi:10.1016/j.ijhydene.2010.02.001.

[6] H. Quack, Conceptual design of a high efficiency large capacity hydrogen liquefier, AIP Conference Proceedings 613 (2002) 255. doi:10.1063/1.1472029.

[7] G. Valenti, E. Macchi, Proposal of an innovative, high-efficiency, large-scale hydrogen liquefier, International Journal of Hydrogen Energy 33 (2008) 3116–3121. doi:10.1016/j.ijhydene.2008.03.044.

[8] Report on technology overview and barriers to energy- and cost-efficient large scale hydrogen liquefaction. FCH JU FP7-JTI Project, Tech. Rep. Ref. 278177 D1.1., IDEALHY Consortium (2012).

[9] U. Cardella, L. Decker, K. H., Economically viable large-scale hydrogen liquefaction, in: Materials science and engineering. Proceedings of the 26th international cryogenic engineering conference and international cryogenic materials conference., 2016.

[10] K. Ohlig, L. Decker, The latest developments and outlook for hydrogen liquefaction technology, AIP Conference proceedings 1573 (2015) 1311. doi:10.1063/1.4860858.

[11] M. Lipman, H. Cheung, O. P. Roberts, Continuous conversion hydrogen liquefaction, Chemical Engineering Progress 59 (1963) 49–54.

[12] H. L. Hutchinson, L. F. Brown, P. L. Barrick, A comparison of rate expressions for the low-temperature para-orthohydrogen shift, Advances in Cryogenic Engineering 16 (1970) 96–103.

[13] H. L. Hutchinson, P. L. Barrick, L. F. Brown, Experimental study of reaction kinetics for para-orthohydrogen at 20 to 80 K, Advances in Cryogenic Engineering 10 (1965) 190–196.

[14] H. L. Hutchinson, Analysis of catalytic ortho-parahydrogen reaction mechanisms, Ph.D. thesis, Department of Chemical Engineering, University of Colorado (1966).

[15] D. H. Weitzel, C. C. Van Valin, J. W. Draper, Design data for ortho-parahydrogen converters, Advances in Cryogenic Engineering 3 (1960) 190–196.

[16] J. P. Maegher, Modeling hydrogen liquefiers with kinetic conversion of ortho to para hydrogen in plate-fin heat exchangers, Master's thesis, State University of New York (2008).

[17] M. L. Michelsen, J. M. Mollerup, Thermodynamic models: Fundamentals and computational aspects, 2nd Edition, Tie-Line Publictions, Holte, Denmark, 2007.

[18] Ø. Wilhelmsen, G. Skaugen, M. Hammer, P. E. Wahl, J. C. Morud, Time Efficient Solution of Phase Equilibria in Dynamic and Distributed Systems with Differential Algebraic Equation Solvers, Ind. Eng. Chem. Res. 52 (2013) 2130.

[19] Ø. Wilhelmsen, A. Aasen, G. Skaugen, P. Aursand, A. Austegard, E. Aursand, M. Aa. Gjennestad, H. Lund, G. Linga, M. Hammer, Thermodynamic modeling with equations of state: present challenges with established methods, Industrial & Engineering Chemistry Research 56 (2017) 3503–3515. doi:10.1021/acs.iecr.7b00317.

[20] D.-Y. Peng, D. B. Robinson, A new two-constant equation of state, Industrial & Engineering Chemistry Fundamentals 15 (1) (1976) 59–64. doi:10.1021/i160057a011.

[21] R. Manglik, A. Bergels, Heat transfer and pressure drop correlations for the rectangular offset strip fin compact heat exchanger, Experimental Thermal and Fluid Science 10 (2) (1995) 171–180. doi:10.1016/0894-1777(94)00096-Q.

[22] R. B. Bird, W. E. Stewart, E. N. Lightfoot, Transport Phenomena, John Wiley & Sons, New York, 2007.

[23] V. Gnielinski, New equations for heat and mass transfer in the turbulent flow in pipes and channels, Forschung im Ingenieurwesen 41 (1975) 8–16.

[24] F. K. Filonenko, Hydraulic resistance in pipes (in Russian), Teploenergetika 1 (1954) 40 – 44.

[25] J. E. Hesselgreaves, Compact Heat Exchangers, Pergamon Press, Oxford, 2001.

[26] D. L. Bennett, C. J. C., Forced convective boiling in vertical tubes for saturated pure components and binary mixtures, AIChe Journal 26 (1980) 451–461.

[27] H. K. Forester, N. Zuber, Dynamics of vapor bubble growth and boiling heat transfer, AIChe Journal 1 (1955) 531–535.

[28] B. L. D., G. N. Kruzhilin, Heat transfer and hydraulic resistance during condensation of steam in a horizontal tube and in a bundle of tubes, Int. J. Heat and Mass Transfer 10 (1967) 361–373.

[29] L. Silver, Gas cooling with aqueous condensation, Trans. Inst. Chem. Eng. 25 (1947) 30–47.

[30] J. K. Bell, M. A. Ghaly, An approximate generalized design method for multicomponent/partial condensers, AIChe symp. series. Heat. transfer. 69 (1973) 72–79.

[31] L. Friedel, Improved friction factor pressure drop correlation for horizontal and vertical two phase pipe flow, in: European Two Phase Flow Group Meeting, ISPRA, Vol. 18, 1979, pp. 485–491.

[32] M. H. Wesenberg, Gas heated steam reformer modelling, Ph.D. thesis, Department of Chemical Engineering, Norwegian University of Science and Technology (2006).

[33] P. E. Peters, R. S. Schiffino, P. Harriott, Heat transfer in packed-tube reactors, Industrial & Engineering Chemistry Fundamentals 27 (1988) 226–233. doi:10.1021/ie00074a003.

[34] R. E. Hicks, Pressure drop in packed beds of spheres, Industrial & Engineering Chemistry Fundamentals 9 (3) (1970) 500–502.

[35] S. Kjelstrup, D. Bedeaux, Non-Equilibrium Thermodynamics of Heterogeneous Systems, World Scientific, Singapore, 2008.

[36] Ø. Wilhelmsen, E. Johannessen, S. Kjelstrup, Energy efficient reactor design simplified by second law analysis, International Journal of Hydrogen Energy 35 (2011) 13219–13231.

[37] C. K. Heck, P. L. Barrick, Liquid-Vapor Equilibria of the Neon-Helium System, Springer US, Boston, MA, 1967, pp. 714–718.

[38] M. Knorn, Vapor-liquid equilibria of the neon-helium system, Cryogenics 19 (1967) 177.

[39] A. Aasen, M. Hammer, G. Skaugen, J. Jakobsen P., Ø. Wilhelmsen, Thermodynamic models to accurately describe the PVTxy-behavior of water/carbon dioxide mixtures, Fluid Phase Equilibria 442 (2017) 125–139. doi:10.1016/j.fluid.2017.02.006.

[40] G. Valenti, E. Macchi, S. Brioschi, The influence of the thermodynamic model of equilibrium-hydrogen on the simulation of its liquefaction, International Journal of Hydrogen Energy 37 (2012) 10779–10788. doi:10.1016/j.ijhydene.2012.04.050.